

# Chaos and mixing in self-propelled droplets

Reiner Kree<sup>1</sup> and Annette Zippelius<sup>1</sup>

<sup>1</sup>University Göttingen, D-37077 Göttingen, Germany

(Dated: May 30, 2022)

We consider self-propelled droplets which are driven by internal flow. Tracer particles, which are advected by the flow, in general follow chaotic trajectories, even though the motion of the autonomous swimmer is completely regular. The flow is mixing, and for Péclet and Batchelor numbers, which are realized e.g. in eucaryotic cells, advective mixing can substantially accelerate and even dominate transport by diffusion.

Fluid flow in small droplets or vesicles is essential for many biological and chemical processes, both in artificially fabricated microdroplets and in biological cells. Droplet microfluidics [1, 2] has a rapidly growing range of applications including molecular detection, imaging, drug delivery and diagnostics. It has also been used to synthesize artificial cells, using droplet stabilized vesicles which can be filled with filaments and motors in a controlled way [3]. Furthermore, viscous liquid droplets, which are chemically driven out of equilibrium, have been shown to grow and divide, reminiscent of living cells [4].

Both artificial and biological cells contain active matter, which can generate intracellular flow, which in turn leads to a variety of functions, ranging from transport of nutrients [5, 6] to control of asymmetric cell division [7] and to cell locomotion [8]. The internal flow in droplets and cells is experimentally accessible with the help of tracer particles which are advected by the flow. Several techniques and a variety of tracers are available [9, 10]. Recently it has become possible to perturb cytoplasmic flow locally, in vivo and probe-free by an interactive microscopic technique [7], which allows to simultaneously observe the consequences of such perturbations.

Among the many possible functions of internal flow is the advection of particles, which gives rise to stirring and mixing as important prerequisites for biochemical reactions. In microdroplets, laminar creeping flow often persists, and mixing by diffusion is inefficient on reaction time scales. In droplet-based microfluidics several techniques have been developed to rapidly mix the particle content by an externally generated flow. Stirring by chaotic advection due to simple Eulerian flow fields has been extensively studied in the past (for a recent review see [11]). The first example of an incompressible flow field inside a sphere, which leads to chaotic Lagrangian trajectories was given in Ref. [12]. In Ref. [13] it was shown that simple linear flow fields in the ambient fluid may generate stirring by chaotic advection in passive droplets. In eukaryotic cells, one observes intracellular flow, known as cytoplasmic streaming, which is generated for example by molecular motors, carrying cargo and entraining the adjacent fluid. Advection of chemicals by the flow contributes significantly to molecular transport and mixing [5, 6]. The complex architecture of a biological cell is of course not adequately captured by a liquid droplet and many other mechanisms are known to contribute to

transport in a cell. Nevertheless such a simple model as a self-propelled droplet can be a first approximation to study the chaotic flow generated by active matter in biological cells. It may furthermore prove useful for efforts to synthesize cells from a small number of components.

In the present work, we consider autonomous self-propelled droplets, driven by an internal flow. We show that the trajectories of particles advected by this flow display the full richness of dynamical systems, ranging from stagnation points and closed orbits to quasi-periodic motion and chaos [11, 12]. Self-generated flow provides an efficient mechanism for stirring and mixing inside the droplet, while the motion of the droplet as a whole remains simple and regular, e.g. rectilinear or along a helix.

We study spherical droplets of radius  $a = 1$ , built from two immiscible fluids and driven either by active body force distributions,  $\mathbf{f}^{act}$  inside the droplet or by active surface tractions  $\mathbf{t}^{act}$  on the interface. The forcing mechanism generates flow  $\mathbf{v}(\mathbf{r})$  in the interior of the droplet, which in turn generates flow in the surrounding fluid and gives rise to self-propulsion. We have computed such flow fields for a spherical droplet and general forcing in Stokes approximation [8], i.e. the solution of

$$\eta \nabla^2 \mathbf{v} - \nabla p = -\mathbf{f}^{act}, \quad \nabla \cdot \mathbf{v} = 0. \quad (1)$$

If the forcing is achieved by tractions, then  $\mathbf{f}^{act} = 0$  and force balance at the interface has to include active tractions  $\mathbf{t}^{act}$ . Self-propulsion requires that the total force and torque exerted by the fluid on the droplet vanishes.

The internal flow implies a constant nonzero linear and angular momentum of the droplet which determine its linear and angular velocity,  $\mathbf{U} = \frac{3}{4\pi} \int_V \mathbf{v}(\mathbf{r}) d^3r$  and  $\boldsymbol{\omega} = \frac{15}{8\pi} \int_V d^3r \mathbf{r} \times \mathbf{v}$ , of self-propulsion. The simplest such flow field due to active tractions, which propels the droplet in  $\hat{\mathbf{n}}$ -direction takes on the form

$$\mathbf{v}_t(\mathbf{r}) = (1 - 2r^2)\hat{\mathbf{n}} + (\hat{\mathbf{n}} \cdot \mathbf{r})\mathbf{r} \quad (2)$$

in the co-moving frame. A force- and torque-free rotational flow can be written as

$$\mathbf{v}_r(\mathbf{r}) = h(r)\mathbf{r} \times \hat{\boldsymbol{\omega}}. \quad (3)$$

with the unit vector  $\hat{\boldsymbol{\omega}} = \boldsymbol{\omega}/|\boldsymbol{\omega}|$  pointing in the direction of angular momentum. Such a flow cannot be generated by tractions but needs chiral body forces. For details see

[8], where we also derived admissible functional forms of  $h(r)$ . All these flows must vanish on the interface. For the present work, we have chosen  $h(r) = -1 + 3r^2 - 2r^3$  as a simple illustrating example. Advected particles subjected to a linear combination of  $\mathbf{v}_t$  and  $\mathbf{v}_r$  follow the equation of motion  $\frac{d\mathbf{r}}{dt} = a_t \mathbf{v}_t(\mathbf{r}) + a_r \mathbf{v}_r(\mathbf{r})$ , which constitutes a three dimensional, non-linear dynamical system in the interior of a sphere. In the following we first introduce axially symmetric regular flow fields characterised by  $\hat{\mathbf{n}} = \hat{\boldsymbol{\omega}}$ . This idealised situation is perturbed either by a time-independent biaxiality ( $\hat{\mathbf{n}} \neq \hat{\boldsymbol{\omega}}$ ) or by a time-periodic direction  $\hat{\mathbf{n}}(t)$ . We discuss that both perturbations, taken separately or in combination, give rise to chaotic trajectories and to mixing.

For  $\hat{\mathbf{n}} = \hat{\boldsymbol{\omega}} = \hat{\mathbf{z}}$  the equations of motion in cylindrical coordinates  $x = \varrho \cos \phi$ ,  $y = \varrho \sin \phi$ ,  $\varrho = \sqrt{x^2 + y^2}$  take on the form

$$\begin{aligned} \frac{d\varrho}{dt} &= a_t z \varrho \\ \frac{dz}{dt} &= a_t (1 - 2\varrho^2 - z^2) \\ \frac{d\phi}{dt} &= -a_r h(\varrho, z), \end{aligned} \quad (4)$$

which implies the conservation of angular momentum  $L_z$  due to axial symmetry. As for any two-dimensional incompressible flow, the first two equations can be mapped onto Hamiltonian dynamics. For our case the Hamiltonian becomes  $H = a_t(p^2 + pq^2 - p)$  with  $q = z, p = \varrho^2$ .

For  $a_r = 0$  (and thus  $L_z = 0$ ) the trajectories in the x-z plane are shown in the left part of Fig.1. Also shown are the hyperbolic stagnation points at the poles, and the two elliptic stagnation points at  $z = 0$ ,  $\varrho = \pm 1/\sqrt{2}$ , which span a whole circle of stagnation points in the x-y plane due to the axial symmetry. For any other choice of  $\hat{\mathbf{n}} = \hat{\boldsymbol{\omega}}$ , the flow pattern is a rotated version of Fig.1a. If the strength of the forcing and thus  $a_t(t)$  is time-dependent, this can be absorbed into a rescaled time  $\tau$  with  $d\tau/dt = 1/a_t(t)$  without changing the streamlines and the shape of the droplet's trajectory. In the following, we put  $a_t = 1$ .

For  $a_r \neq 0$  the angular momentum  $L_z$  is still conserved, but no longer vanishes. Every trajectory results from a superposition of two periodic motions, one in the x-z plane due to  $\mathbf{v}_t$  and one in the x-y plane due to  $\mathbf{v}_r$ , which leads to periodic or quasi-periodic motion on tori. It is plausible and can be shown that these tori constitute a complete foliation of the sphere.

Now consider trajectories of advected particles, which are generated by time-independent forcing for which the translational and angular velocities are *no longer parallel*. As a consequence, the system is not axially symmetric and the trajectories are determined by a fully coupled, autonomous system of three differential equations. There are two control parameters of this flow:  $a_r$  and  $\hat{\mathbf{n}} \cdot \hat{\boldsymbol{\omega}} = \cos \theta$ . To illustrate the transition to chaos, we choose  $\hat{\mathbf{n}} = \hat{\mathbf{z}}$  and  $\hat{\boldsymbol{\omega}}$  tilted by an angle  $\theta$  with respect to the z-axis in the x-z plane. In Fig.2, we show Poincaré

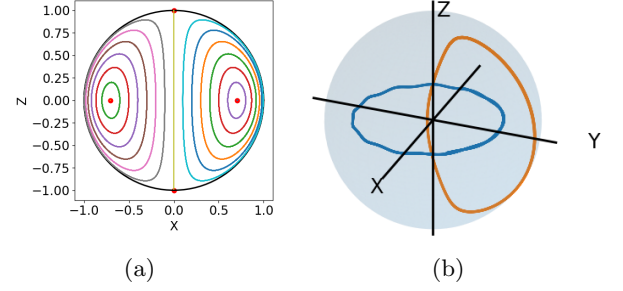


FIG. 1. (a): Trajectories of tracer particle inside a droplet, which moves with constant linear velocity and without rotation. Initial conditions are  $\mathbf{r}(0) = \pm k \cdot 10^{-1} \hat{\mathbf{x}}$  with  $k = 1, \dots, 6$  (b): a 3d graph of the cycles for  $\hat{\boldsymbol{\omega}}$  tilted with respect to  $\hat{\mathbf{z}}$  by  $\theta = 0.3\pi$  (see also Fig.2)

sections of this flow for  $\theta = 0.3\pi$  and different  $a_r$ . For small values of  $a_r$ , we find regular motion for all values of  $\theta$ . A finite tilt of the  $\hat{\boldsymbol{\omega}}$  axis causes a new cycle to appear, corresponding to 2-periodic points in the Poincaré section, see Fig.2. Now there are two types of tori (A and B), winding around the two cycles shown in Fig.1 b. Type A wind around the cycle, which continuously emerges from the line of fixpoints at  $a_r = 0$ , and type B tori enclose the new cycle. The topology of the flow is controlled by these coherent structures and the vanishing of the rotational velocity and the radial part of the translational velocity on the interface. This latter feature is a general property of *all* force- and torque-free flows inside the sphere. Thus advected particles on the surface always follow regular trajectories connecting the two poles. In terms of dynamical system theory, the droplet's surface is the unstable manifold of the south pole and the stable manifold of the north pole, which are hyperbolic fixpoints. The rotational flow also vanishes on the axis of rotation, which therefore is clearly visible in the Poincaré sections. With increasing  $a_r$  tori of both types decay and chaotic trajectories as well as islands of regular motion appear. We stress that the motion of the droplet as a whole is still simple. If we assume that the time-independent forcing is co-translating and co-rotating with the interior fluid, then the droplet moves on a helix – even in the presence of chaotic streamlines inside. (For a detailed discussion of the droplet's trajectories in dependence on the internal flow see Ref.[8]).

In biological systems the active elements such as motors in a vesicle or cell, are in general time dependent. Of particular interest is a time-periodic forcing. Here, we consider a droplet without rotational flow but with periodic changes in the droplet's swimming direction,  $\hat{\mathbf{n}}(t) = \hat{\mathbf{r}}(\theta(t), \varphi(t))$ , parametrised by polar and azimuthal angles  $\theta(t)$  and  $\varphi(t)$ . If we choose  $\varphi(t) = 0$  the  $\hat{\mathbf{n}}$ -axis always stays in the x-z plane. It is easy to see by direct inspection of the equations of motion that trajectories starting with  $y = 0$  remain in the x-z plane, which thus constitutes a 2d invariant manifold of the 3d flow. Con-

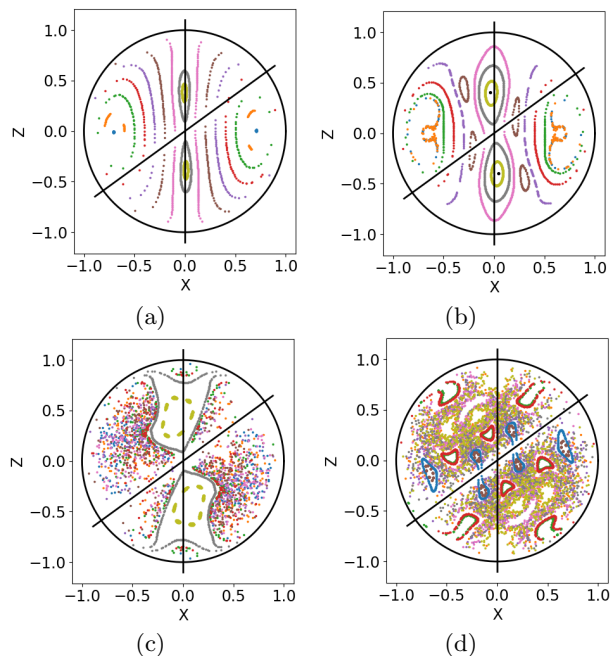


FIG. 2. Poincaré section ( $x$ - $z$  plane) of time-independent flow with  $\hat{\mathbf{n}} = \hat{\mathbf{z}}$  and  $\hat{\omega}$  tilted as indicated in the figure for different strength of the rotational flow,  $a_r = 1.1$  (a), 2 (b), 3 (c), 9 (d); initial conditions as used in Fig.1a, with 2 additional trajectories starting on the  $z$ -axis at  $0.1 \cdot \hat{\mathbf{z}}$  and  $0.3 \cdot \hat{\mathbf{z}}$

sequently, the 3d flow originating from initial conditions with  $y > 0$  ( $y < 0$ ) is restricted to the corresponding half-sphere. In the following we consider a simple harmonic time dependence  $\theta(t) = \Delta\theta \cos(t)$  and the same initial conditions ( $y = 0$ ) as those shown in Fig.1a. Stroboscopic views (at  $t_k = 2\pi k$ ) of trajectories are shown in Fig.3 for increasing amplitude  $\Delta\theta$ . For small  $\Delta\theta$  we observe coexistence of regular motion and chaotic trajectories, but regular orbits gradually disappear for larger tilt. The flow within the 2d invariant manifold represents an example of the classical scenario of emerging chaotic behavior in a periodically driven Hamiltonian system in a 2d phase space[14]. The onset of chaos does not affect the motion of the droplet as a whole, which is a simple translational motion following the oscillation of  $\hat{\mathbf{n}}(t)$ .

The chaotic trajectories provide an efficient internal mechanism for mixing, which may accelerate intracellular processes like signal transduction, as we now discuss. There are mathematical definitions of perfect mixing in ergodic theory [14], but there is no unique measure of the efficiency of mixing. Here we focus on a simple generic scenario as it may arise in signal transduction,— the temporal development of a chemical signal of  $N$  initially neighbouring particles. An example is shown in Fig.4 for the 2-dimensional flow described above. Mixing efficiency is characterised by the dispersal of the initial signal for times up to a finite  $t_{max}$ , which is set by reaction times, life times of active states or other relevant scales. Stretching, folding and stirring is capable to transport a chemical

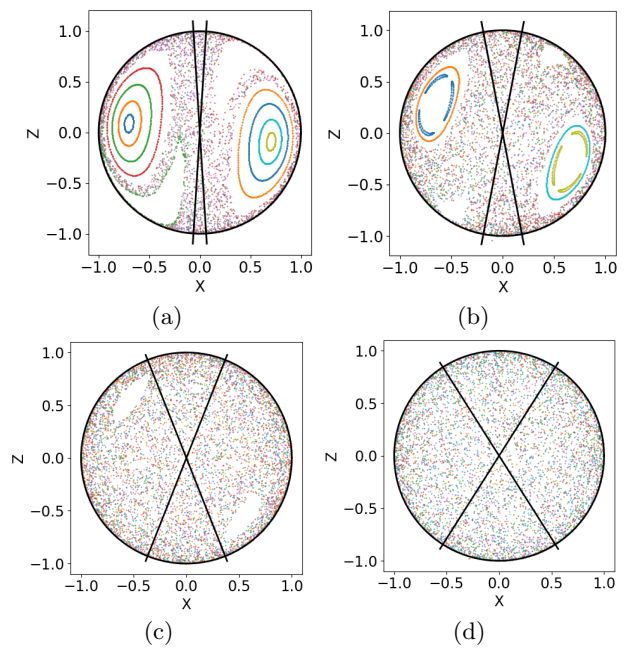


FIG. 3. Stroboscopic views for a flow due to time-dependent  $\hat{\mathbf{n}}$  (see text); tilt angles  $\Delta\theta = k\pi/180$  with  $k=4$  (a), 10 (b), 20 (c) and 30 (d) for same initial conditions as in Fig.2a

signal over the droplets diameter within a few periods of oscillation, while at the same time it leads to a distribution of large concentration gradients, as seen in Fig.4a. Once several such stretching and folding processes have taken place (see Fig.4b), diffusive transport is expected to take over and generate a homogeneous distribution in a cell or vesicle of size in the  $\mu\text{m}$  range (see below.) Note, however that not all trajectories are chaotic in Fig.3. We also observe regular islands, and if the initial distribution is chosen within such an island it does not mix, as illustrated in Fig.4d. Regions of chaotic advection are thus separated from regular motion by transport barriers, which can only be surmounted by diffusion. In this way the droplets interior is subdivided dynamically into mixing and non-mixing regions, which can be controlled via parameters of the flow. An active droplet can thus easily switch from a mixing to a partially mixing or non-mixing state, by changing its global activities, like e.g.,  $\Delta\theta$  or the velocity scales  $a_r$  and  $a_t$  of chiral and non-chiral flow.

So far we have discussed mixing in the  $x$ - $z$  plane, which constitutes an invariant manifold of the flow. Mixing in 3d can be achieved by either choosing the initial conditions outside the invariant manifold or by adding a rotational flow. In the former case, the invariant manifold constitutes a barrier between the  $y > 0$ - and the  $y < 0$ -half-sphere. Fig. 5a is the analogue of Fig. 4c for an initial distribution in a cube centered at  $\mathbf{r}_0 = (0.6, 0.1, 0.5)$ . The resulting particle distribution fills the  $y > 0$  half-sphere, however, it is not uniform but accumulates in the neighborhood of the invariant manifold. Mixing within the entire sphere can be achieved with an additional rota-

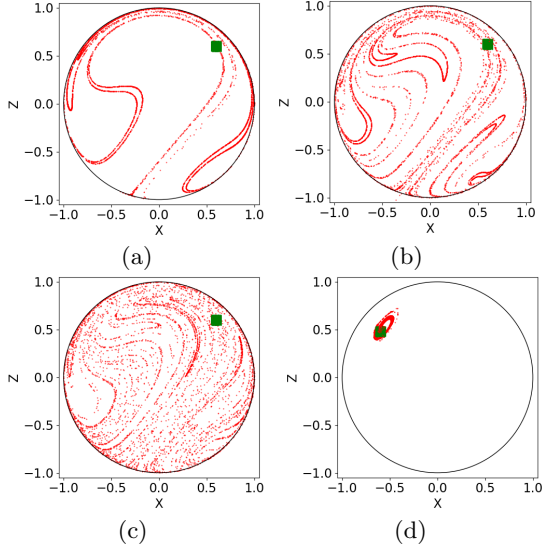


FIG. 4. Temporal development of an initial distribution of  $5 \cdot 10^3$  particles distributed at random within the solid square centered at  $\mathbf{r} = (0.6, 0, 0.6)$  for 3 (a), 4 (b) and 5 (c) periods of  $\theta(t)$ , with  $\Delta\theta = 0.2\pi$ . d) centered at  $\mathbf{r} = (-0.6, 0, 0.5)$  for  $\Delta\theta = 0.12$  after 30 periods of  $\theta(t)$ ,

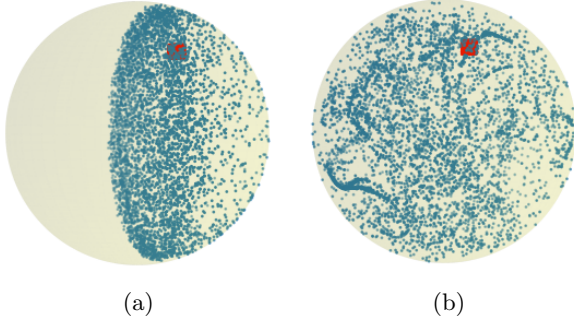


FIG. 5. Positions of  $5 \times 10^3$  particles initially distributed randomly within a small solid cube centered at  $\mathbf{r}_0 = (0.6, 0.1, 0.5)$  after 6 periods of oscillations of  $\hat{\mathbf{n}}(t)$  with  $\Delta\theta = 0.2\pi$  as in Fig. 4a-c. (a) without rotational flow and (b) with rotational flow of strength  $a_r = 1$

tional flow as shown in Fig. 5b. Here the rotational flow of Eq.3 has been added with  $\hat{\omega} = \mathbf{e}_z$  and  $a_r = 1$ . This rotational flow transports the 2d mixing in the invariant manifold into the sphere, and thus leads to effective mixing in 3d.

From the particle distribution we can derive further quantitative statistical measures of mixing by coarse graining. We introduce a partitioning of 2d or 3d space into  $M$  cells with areas or volumes  $\{F_n\}_{n=1}^M$ . In each cell, we count the number of advected particles  $N_n$  and measure the density  $\varrho_n = N_n/(F_n N)$ , which is an estimate of the probability to find a particle in the cell. In order to compare this probability to a uniform distribution, we

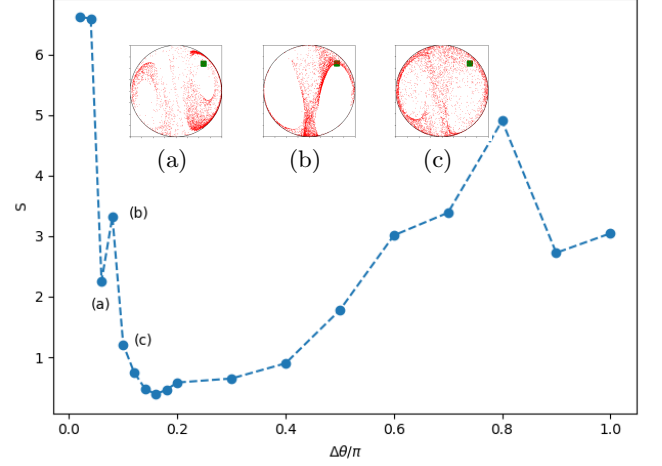


FIG. 6. Coarse grained Kullback-Leibler entropy at  $t = 24\pi$  versus  $\Delta\theta$  for the initial distribution shown in Fig.4a; insets: temporal development as in Fig.4 for 3 selected values (a),(b),(c) of  $\Delta\theta$  and 12 periods of  $\theta(t)$ .

use the Kullback-Leibler (KL) entropy, defined as

$$S = \sum_n \varrho_n \log \frac{\varrho_n}{\varrho} \quad (5)$$

with the uniform density  $\varrho = 1/F$ . Small values of  $S$  indicate good homogeneous mixing properties, whereas large values result from strongly inhomogeneous distributions as, e.g., in Fig.4d.

The KL-entropy depends upon bin sizes and contains statistical errors due to finite  $N$ . We have studied these dependencies and found that  $N \geq 5 \cdot 10^3$  particles and  $\geq 25$  bins in both angular and radial coordinates are sufficient to detect global features of mixing. The entropy is plotted versus  $\Delta\theta$  in Fig.6 after 12 cycles of the axis  $\mathbf{n}$ , which we found to be sufficient to reach a stationary value. The initial conditions have been chosen as in Fig.4a. For small values of  $\Delta\theta \lesssim 0.2$  one observes a decrease of entropy. The decrease is, however, non-monotonic due to Lagrangian coherent structures (like islands, for example), which appear and vanish as  $\Delta\theta$  is varied. This is shown for 3 examples in the inset of Fig.6 a-c. Thus homogenization of an initially localized distribution of particles depends sensitively on  $\Delta\theta$  in accordance with our previous results on single particle trajectories. The coexistence of chaotic regions and regular islands is reflected in correspondingly complex homogenization and mixing properties.

To conclude, flow inside a self-propelling droplet driven by internal active forcing exhibits chaotic advection, which should be observable in an experiment. We stress that the chaotic behavior is predicted for autonomous swimmers, whose trajectories are simple and regular. Although we have illustrated the emergence of chaotic trajectories and their effects on mixing only for a special, self-propelling flow, it is known that there are generic

routes to chaos in 3d incompressible flows [15], and thus we expect most of our qualitative conclusions to hold in a much broader context.

We have investigated the mixing properties of the internal flow by following the time development of an initially localised set of particles, as well as with the help of the Kullback-Leibler entropy. Mixing in microfluidic devices has been studied extensively [16]. Given the reversibility of the flow, mixing is usually achieved with the help of carefully designed geometries or time-dependent external forces. Here, in contrast, we consider spherical shapes only and show that internal forcing mechanisms result in mixing. How relevant are these results on scales of biological cells where molecules or vesicles need to be transported? Can chaotic advection beat transport or mixing by diffusion? As a hint, we estimate two dimensionless numbers for an internal fluid with a viscosity  $\eta$ . For directed transport, the Péclet number  $Pe = UL/D$  gives the ratio of convective to diffusive transport. Here,  $U$  denotes a typical velocity,  $L$  the size of the cell, and for an object of radius  $R$  we estimate the diffusion constant  $D = k_B T / 6\pi\eta R$  with help of the Einstein relation. Assuming  $\eta$  to be 4 times the viscosity of the ambient water we find  $Pe/(ULR) \approx 6\pi s/\mu m^3$ . The extension of a diffusing protein is estimated as  $R \sim 10 nm$ . For a bacterium of typical cell size  $L \sim 1 \mu m$ , one needs a velocity of  $U \sim 5 \mu m/s$  to achieve  $Pe = 1$ . On the other hand, a eukaryotic cell can be as large as  $L \sim 100 \mu m$ , implying  $Pe \sim 100$  for the same velocity. A typical scale, which compares mixing by stretching and folding to diffusion is the Batchelor length  $l_B = \sqrt{D/\lambda}$ . For distances smaller than  $l_B$  mixing is dominated by diffusion [11]. Here  $\lambda$  denotes a positive Liapunov exponent, which characterizes the spreading of two nearby initial conditions:  $\delta x \sim e^{\lambda t}$ . We found that  $\lambda \sim 1/s$  for the studied chaotic flows with typical velocities of  $1 \mu m/s$  so that  $l_B \sim 1 \mu m$ . Thus chaotic advective transport in an autonomous microswimmer provides an efficient mechanism for mixing in case diffusion is slow due to the large size of either the advected object or the cell. Even for small sized objects or cells, the rapid buildup of large gradients due to stretching and folding can accelerate diffusive transport substantially.

## APPENDIX

In this appendix, we briefly recall the computation of the flow fields inside the droplet, and in particular the rotational flow of Eq.3, which cannot be generated by surface tractions but requires the action of body forces. For details of the calculations we refer to [8].

Consider a neutrally buoyant spherical droplet of radius  $R = 1$ , filled with an incompressible Newtonian fluid of viscosity  $\eta$ , which is swimming in another Newtonian fluid of viscosity  $\eta_a$  and driven by internal active volume force densities  $\mathbf{f}(r, \theta, \varphi)$  and/or active surface force densities  $\mathbf{t}(\theta, \varphi)$  on the interface at  $r = R$ . The forces

generate a flow field inside the droplet, which is coupled to the ambient fluid via viscous forces at the interface and may lead to self-propulsion. To calculate the flow field  $\mathbf{v}$  in the lab frame we choose a spherical coordinate system  $(r, \theta, \varphi)$  with its origin at the center of the droplet at a fixed time  $t$ . The unit vectors corresponding to the coordinate lines are denoted by  $\mathbf{e}_r, \mathbf{e}_\theta, \mathbf{e}_\varphi$ .

For small Reynolds number, the flow obeys Stokes' equations

$$\eta(r)\nabla^2\mathbf{v} = -\nabla p + \mathbf{f}; \quad \nabla \cdot \mathbf{v} = 0 \quad (6)$$

with  $\eta(r < 1) = \eta$  and  $\eta(r > 1) = \eta_a$ . To distinguish the internal from the ambient flow we introduce  $\mathbf{v}(r > 1) = \mathbf{v}_a$ . For immiscible fluids and no interfacial velocity slip,  $\mathbf{v}$  is continuous across the interface,

$$\mathbf{v}(r = 1, \theta, \varphi) = \mathbf{v}_a(r = 1, \theta, \varphi). \quad (7)$$

Furthermore every surface element of the interface is force free, which implies

$$(\boldsymbol{\sigma}(\mathbf{v}_a) - \boldsymbol{\sigma}(\mathbf{v}) - \mathbf{t}) \cdot \mathbf{e}_r = 2\gamma\mathbf{e}_r. \quad (8)$$

The viscous stress tensor  $\boldsymbol{\sigma}$  is characterized by its cartesian components  $\sigma_{ij}(\mathbf{v}) = -p\delta_{ij} + \eta(\partial_i v_j + \partial_j v_i)$  with pressure field  $p(r, \theta, \varphi)$ . The term on the r.h.s. of Eq. 8 results from a homogeneous surface tension  $\gamma$ .

To take advantage of the spherical geometry, we expand the pressure field into spherical harmonics  $Y_{\ell m}$  and the vector fields  $\mathbf{v}, \mathbf{f}$  and  $\mathbf{t}$  into vector spherical harmonics. Our choice for the latter is  $\mathbf{Y}_{\ell m}^{(0)} = Y_{\ell m}\mathbf{e}_r$ ,  $\mathbf{Y}_{\ell m}^{(1)} = r\nabla Y_{\ell m}$  and  $\mathbf{Y}_{\ell m}^{(2)} = \mathbf{r} \times \nabla Y_{\ell m}$ . Inserting the expansion

$$\mathbf{v}(r, \theta, \varphi) = \sum_{s=0}^2 \sum_{\ell=0}^{\infty} \sum_{m=-\ell}^{\ell} v_{\ell m}^s(r) \mathbf{Y}_{\ell m}^{(s)}(\theta, \varphi) \quad (9)$$

and the corresponding expansions for  $p, \mathbf{f}$  and  $\mathbf{t}$  into Stokes equations results in a system of ordinary differential equations for  $v_{\ell m}^s(r)$ , which is completely decoupled in  $\ell$  and  $m$ . For each  $\ell, m$  the only remaining coupling is between  $s = 0$  and  $s = 1$  modes.

The simple translational flow of Eq.2 represents the  $m = 0$  component of the nonchiral part of Eq.9 ( $s = 0, 1$ )

$$\begin{aligned} \mathbf{v}_t(\mathbf{r}) &= \mathbf{v}(\mathbf{r}) - \mathbf{U} \\ &\propto (r^2 - 1)\mathbf{Y}_{10}^{(0)}(\theta, \varphi) + (2r^2 - 1)\mathbf{Y}_{10}^{(1)}(\theta, \varphi) \\ &\propto (r^2 - 1)\cos\theta\mathbf{e}_r + (1 - 2r^2)\sin\theta\mathbf{e}_\theta \end{aligned}$$

in agreement with Eq.2. The rotational flow represents the chiral part of Eq.9 ( $s = 2$ ). Traction forces give rise to rigid body motion which is not compatible with the vanishing of the total torque as required for autonomous swimming. Body forces on the other hand can give rise to rotational flow inside the droplet. The simple example, discussed in the main text, corresponds to the force density  $\mathbf{f}(\mathbf{r}) = \sum_m \gamma_m(r) \mathbf{Y}_{1m}^{(2)}(\theta, \varphi)$ . Let us first consider the axially symmetric case with only the  $m = 0$

component of the force density. The total torque vanishes, if  $\int_0^1 dr r^3 \gamma_0(r) = 0$ . This can be achieved by two power laws for  $\gamma_0(r)$ , for example  $\gamma_0(r) = c_1 r + c_2 r^2$  with  $c_1/5 = -c_2/6$ . The resulting rotational flow is given by

$$\begin{aligned} \mathbf{v}_r(\mathbf{r}) &\sim ((r - r^3)/2 + (r - r^4)/3) \mathbf{r} \times \nabla Y_{10}(\theta, \varphi) \\ &\sim h(r) \sin \theta \mathbf{e}_\phi = -h(r) \mathbf{r} \times \mathbf{e}_z. \end{aligned} \quad (10)$$

The more general case with all  $\gamma_m(r)$  of the same functional form, can then be shown [8] to result in  $\mathbf{v}_r(\mathbf{r}) \sim -h(r) \mathbf{r} \times \hat{\boldsymbol{\omega}}$ .

- 
- [1] S.Y. Teh, R. Lin, L.H. Hung, and A.P. Lee, “Droplet microfluidics,” *Lab Chip* **8**, 198–220 (2008).
  - [2] W.L. Chou, P.Y. Lee, C.L. Yang, W.Y. Huang, and Y.S. Lin, “Recent advances in applications of droplet microfluidics,” *Micromachines* **6** (2015).
  - [3] M. Weiss, J.P. Frohnmayer, L.T. Benk, B. Haller, J.W. Janiesch and T. Heitkamp, M. Börsch, R.B. Lira, R. Dimova, R. Lipowsky, E. Bodenschatz, J.C. Baret, T. Vidakovic-Koch, K. Sundmacher, I. Platzman, and J.P. Spatz, “Sequential bottom-up assembly of synthetic cells,” *Nature Mat.* **17**, 89–96 (2017).
  - [4] D. Zwicker, R. Seyboldt, C. A. Weber, A. A. Hyman, and F. Jülicher, “Growth and division of active droplets provides a model for protocells,” *Nature Phys.* **13**, 408–413 (2014).
  - [5] Jan-Willem van de Meent, Idan Tuval, and Raymond E. Goldstein, “Nature’s microfluidic transporter: rotational cytoplasmic streaming at high peclet number,” *Phys. Rev. Lett.* **101**, 178102 (2008).
  - [6] Raymond E. Goldstein and Jan-Willem van de Meent, “A physical perspective on cytoplasmic streaming,” *Interface focus* **5**, 20150030 (2015).
  - [7] M. Mittasch, P. Gross, M. Nestler, A.W. Fritsch, Ch. Isermann, M. Kar, M. Munder, A. Voigt, S. Alberti, W. Grill, and M. Krysing, “Non-invasive perturbations of intracellular flow reveal physical principles of cell organization,” *Nature Cell Biol.* **20**, 344–351 (2018).
  - [8] R. Kree, P.S. Burada, and A. Zippelius, “From active stresses and forces to self-propulsion of droplets,” *J. Fluid Mech.* **821**, 595–623 (2017).
  - [9] Kinneret Keren et al., “Intracellular fluid flow in rapidly moving cells,” *Nature cell biology* **11**, 1219 (2009).
  - [10] D. Arcizet et al., “Temporal analysis of active and passive transport in living cells,” *Phys. Rev. Lett.* **101**, 248103 (2008).
  - [11] H. Aref et al., “Frontiers of chaotic advection,” *Rev. Mod. Phys.* **89**, 025007 (2017).
  - [12] K. Bajer and H. K. Moffatt, “On a class of steady confined stokes flow with chaotic streamlines,” *J. Fluid Mech.* **212**, 337 (1990).
  - [13] H.A. Stone, A. Nadim, and S.H. Strogatz, “Chaotic streamlines inside drops immersed in steady stokes flow,” *J. Fluid. Mech.* **232**, 629–646 (1991).
  - [14] V.I. Arnol’d and A. Avez, *Ergodic problems of classical mechanics* (Addison-Wesley, 1989).
  - [15] I. Mezic and S. Wiggins, “On the integrability and perturbation of three-dimensional fluid flows with symmetry,” *J. Nonlinear Sci.* **4**, 157 (1994).
  - [16] Chai-Yen Lee et al, “Microfluidic mixing: a review,” *Int. J. Mol. Sci.* **12**, 3263 (2011).